Optimal transient disturbances behind a circular cylinder in a quasi-two-dimensional magnetohydrodynamic duct flow

Wisam K. Hussam, Mark C. Thompson, and Gregory J. Sheard

Related Articles

Additional information on Phys. Fluids

Optimal transient disturbances behind a circular cylinder in a quasi-two-dimensional magnetohydrodynamic duct flow

Wisam K. Hussam,[a] Mark C. Thompson, and Gregory J. Sheard[b]
*Department of Mechanical and Aerospace Engineering, Monash University,
Victoria 3800, Australia*

The transient response of optimal linear perturbations of liquid metal flow under a strong axial magnetic field in an electrically insulated rectangular duct is considered. The focus is on the subcritical regime, below the onset of von Kármán vortex shedding, to determine the role of optimal disturbances in developing wake instabilities. In this configuration, the flow is quasi-two-dimensional and can be solved over a two-dimensional domain. Parameter ranges considered include Reynolds numbers $50 \leq Re \lesssim 2100$, modified Hartmann numbers $50 \leq Ha^\star \lesssim 500$, and blockage ratios $0.1 \leq \beta \leq 0.4$. In some instances, the optimal disturbances are found to generate energy growth of greater than four orders of magnitude. Variation in the wake recirculation length in the steady flow regime is determined as a function of Reynolds number, Hartman number, and blockage ratio, and a universal expression is proposed. For all β, the energy amplification of the disturbances is found to decrease significantly with increasing Hartmann number and the peak growth shifts towards smaller times. The optimal initial disturbances are consistently located in the vicinity of the boundary layer separation from the cylinder, and the structure of these disturbances is consistent for all Hartmann numbers and blockage ratios considered in this study. The time evolution of the optimal perturbations is presented, and is shown to correspond to sinuous oscillations of the shear layer downstream of the wake recirculation. The critical Reynolds number for the onset of growth at different Hartmann numbers and blockage ratios is determined. It is found that it increases rapidly with increasing Hartmann number and blockage ratio. For all β, the peak energy amplification grows exponentially with Re at low and high Hartmann numbers. Direct numerical simulation in which the inflow is perturbed by a random white noise confirms the predictions arising from the transient growth analysis: that is, the perturbation excites and feeds energy into the global mode. © *2012 American Institute of Physics.*
[http://dx.doi.org/10.1063/1.3686809]

I. INTRODUCTION

Magnetohydrodynamic flows through ducts under a uniform transverse magnetic field are important due to practical applications such as magnetohydrodynamic generators, pumps, metallurgical processing, and fusion reactors. In fusion reactors, liquid metal may be used as a coolant and as a breeder material.[1] It circulates within the blanket and is exposed to a strong magnetic field used to confine the plasma. As a result, electric currents are induced within the conducting fluid. These currents in turn are subject to a Lorentz force due to the magnetic field, which causes changes to the velocity profile and turbulence characteristics, and it exerts a retarding force on the flow. For a strong magnetic field the flow is laminar, as velocity fluctuations in the direction of the magnetic field are strongly suppressed, and heat transfer in the ducts of the blanket, where a large amount of

---

[a]Electronic mail: Wisam.alSaadi@monash.edu.
[b]Electronic mail: Greg.Sheard@monash.edu.

heat must be removed, is significantly decreased.[2] However, vortices parallel to the magnetic field are not completely damped.[3] The unsteadiness of these flow structures could be utilized to enhance heat transfer, which could be induced by using turbulence promoters such as a circular or rectangular cylinder placed inside the duct of a blanket. This approach has been investigated experimentally[4–7] and numerically.[8–10] For the case with insulated wall duct, Refs. 10 and 11 demonstrated that the heat transfer rate under a strong axial magnetic field was improved by more than twice that of the laminar flow.

If the *Hartmann number Ha*, which characterizes the ratio of (electromagnetic/viscous forces)$^{1/2}$ and the *interaction parameter $N = Ha^2/Re$*, which characterizes (electromagnetic/inertial force) are both very high (i.e., $Ha \gg 1$, $N \gg 1$), electromagnetic forces dominate over viscous forces, and the flow in a rectangular duct can be split into a core flow, separated by two thin boundary layers.[12] In the core, there is a balance between pressure gradient and Lorentz force. Viscous effects are confined to the Hartmann layers where the viscosity and Lorentz force come into balance to satisfy the no-slip boundary condition at the walls.[12] The velocity in the core varies only slightly along the magnetic field lines, while in the vicinity of the walls perpendicular to the magnetic field it exhibits an exponential variation. The boundary layer on the walls perpendicular to the magnetic field is known as the Hartmann layer with a thickness that scales as $\delta_H \sim Ha^{-1}$, while the boundary layer along the walls parallel to the magnetic field is known as the Shercliff layer (or side layer), with a thickness that scales as $\delta_S \sim Ha^{-1/2}$.

The effect of the magnetic field on the development of the vortices has been investigated theoretically[13–15] and experimentally.[16–20] The flow characteristics were investigated for decaying grid turbulence,[21] and later for the electromagnetically forced regimes.[22] The key mechanisms are explained by Sommeria and Moreau,[15] who showed that in the core region the velocity components perpendicular to the field are damped by strong joule dissipation, while in the Hartmann layers the turbulent fluctuations are weakly damped in that direction.

The present paper focuses on the role of linear transient growth in the subcritical regime, below the onset of von Kármán vortex shedding, and it consequences for the effective transition to unsteady flow. More specifically, the base flow is linearly stable, though perturbations may exhibit significant transient response. The critical Reynolds numbers for the transition to unsteady flow Re_c in the presence of a magnetic field can be very large; an understanding of the non-modal growth properties of the flow may enable unsteady flow to be invoked at lower Reynolds numbers.

Globally stable flows may still experience significant transient growth of disturbances for some time before they eventually decay to zero.[23] For purely hydrodynamic parallel shear flows ($Ha = 0$), substantial transient growth has been demonstrated for the plane channel,[24] pipe,[25] rectangular duct,[26] and abrupt geometrical expansion flows.[27–30] This growth can be attributed to the non-normality of the eigenmodes associated with many shear flows.[23,31]

For cylinder wake flows without a magnetic field, the adjoint and direct eigenmodes in the region of primary instability have been investigated numerically[31,32] to understand the sensitivity of the flow to external disturbances. More recently, the transient response of the subcritical and supercritical flow has been investigated.[33,34] Reference 35 also studied the transient growth in supercritical and subcritical flow of the circular cylinder wake in an open flow. The transient growth in the subcritical flow of the circular cylinder wake in an open flow has been investigated experimentally[36] using two-dimensional particle image velocimetry. Interestingly, the measured values of transient growth were significantly less than those reported in numerical studies.[34,35]

The effect of an applied magnetic field on the transient growth for the case of steady Hartmann flow, i.e., channel flow of an electrically conducting fluid in the presence of a uniform magnetic field, has been analyzed by a number of authors.[37–39] The optimal modes were found to have the form of streamwise rolls confined to the Hartmann layers. In addition it was found that energy gain of the optimal perturbations is proportional to $(Re/Ha)^2$, and the critical Reynolds number was much higher than for Poiseuille flow.

More recently, Refs. 40 and 41 analyzed the optimal linear growth of perturbations in a rectangular duct with different aspect ratios subjected to a uniform transverse magnetic field. The disturbances of optimal growth are confined to the Shercliff layers. The optimal perturbations are

significantly damped by the magnetic field irrespective of the duct aspect ratio. They concluded that the Hartmann boundary layers perpendicular to the magnetic field do not contribute to the transient growth.

It is unknown how the transient response of a cylinder wake is influenced by the presence of a strong magnetic field for MHD duct flow, and whether this may be exploited to further enhance heat transfer within the duct.

The aim of this paper is to analyze and quantify the transient growth of infinitesimal perturbations in a quasi-two-dimensional magnetohydrodynamic flow past a confined circular cylinder under the influence of a strong magnetic field in the subcritical regime prior to the onset of self-sustained wake oscillations. In particular, the dependence of the transient growth on the Hartmann number and blockage ratio will be investigated and quantified.

II. NUMERICAL METHODOLOGY

The system under investigation is a rectangular duct confining a circular cylinder placed at the center of the duct parallel to the transverse direction and perpendicular to the flow direction. The out-of-plane channel depth is a, and throughout this study, the duct cross-section is taken to have a height to depth ratio $h/a = 2$. The duct walls and the cylinder are assumed to be electrically insulated. A homogeneous magnetic field with a strength B is imposed along the cylinder axis. For a high Hartmann number, the magnetic Reynolds number Re_m, which represents the ratio between the induced and the applied magnetic field is very small. Thus, the induced magnetic field is negligible and the resultant magnetic field is effectively the applied field in the z-direction only. Under these conditions the flow is quasi-two-dimensional and consists of a core region, where the velocity is invariant along the direction of the magnetic field, together with thin Hartmann layers at the walls perpendicular to the magnetic field. The quasi-two-dimensional model has been derived in Ref. 15, by integrating the flow quantities along the magnetic field direction, as shown in Fig. 1.

In this case the non-dimensional magnetohydrodynamic equations of momentum and continuity[9,15] reduce to

$$\frac{\partial \mathbf{u}}{\partial t} = \mathbf{N} - \nabla p + \frac{1}{Re}\nabla^2 \mathbf{u} - 2\frac{d^2}{a^2}\frac{Ha}{Re}\mathbf{u}, \tag{1a}$$

$$\nabla \cdot \mathbf{u} = 0. \tag{1b}$$

Here the non-linear advection term $\mathbf{N} = -(\mathbf{u} \cdot \nabla)\mathbf{u}$, and $\mathbf{u}$ and p are the velocity and pressure, respectively, projected onto the x-y plane. Non-dimensionalization is achieved by scaling lengths by
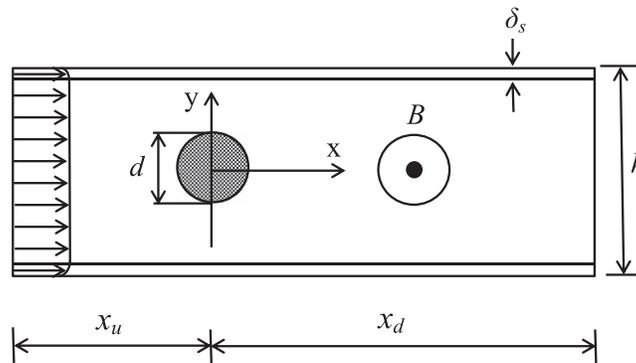
FIG. 1. Schematic diagram of the flow configuration and the extent of the computational domain (not to scale). The magnetic field B acts in the out-of-plane direction, parallel to the cylinder axis. The quasi-two-dimensional approximation models an out-of-plane channel depth of a. Also, δ_S is the thickness of the Shercliff layer, and h and d are the duct width and cylinder diameter, respectively. The blockage ratio $\beta = d/h$. The upstream and downstream lengths are $x_u = 8$ and $x_d = 25$, respectively.

the cylinder diameter d, pressure by ρU_0^2, where ρ is the density and U_0 is the peak inlet velocity, and time by d/U_0.

The dimensionless parameters—the Reynolds and Hartmann numbers—are, respectively, defined as

$$Re = \frac{U_0 \, d}{\nu}$$

and

$$Ha = a \, B \sqrt{\frac{\sigma}{\rho \nu}},$$

where ν, σ, and B are the kinematic viscosity, magnetic permeability of the liquid metal, and the applied magnetic field, respectively. Note that the Hartmann length scale is based on the depth of the channel rather than the cylinder diameter.

It also makes sense to define a *modified Hartmann number*

$$Ha^\star = \frac{d^2}{a^2} Ha,$$

since this non-dimensional parameter defines the relative influence of the magnetic damping term to the viscous diffusion term for the quasi-two-dimensional flow. This variable is important for the current study because the effect of varying blockage ratio, $\beta = d/h$, is examined, i.e., the cylinder diameter (d) is varied while keeping the duct height (h) and depth (a) constant.

The methods applied for examining linear asymptotic stability and transient growth of disturbances are based on time integration of the linearized Navier–Stokes equations.[23,27] These equations are derived by substituting velocity and pressure fields decomposed into a two-dimensional base flow and infinitesimal fluctuating components $\mathbf{u}'(x, y, t)$ and $p'(x, y, t)$. The linearized expansion is based on a steady two-dimensional base flow ($\mathbf{U}$), and the perturbation evolution is described by

$$\frac{\partial \mathbf{u}'}{\partial t} = -\mathrm{DN}\mathbf{u}' - \nabla p' + \frac{1}{Re}\nabla^2 \mathbf{u}' - 2\frac{d^2}{a^2}\frac{Ha}{Re}\mathbf{u}', \tag{2a}$$

$$\nabla \cdot \mathbf{u}' = 0, \tag{2b}$$

where the advection term $\mathrm{DN}\mathbf{u}' = (\mathbf{U} \cdot \nabla)\mathbf{u}' + (\mathbf{u}' \cdot \nabla)\mathbf{U}$.

Let $\mathscr{A}(\tau)$ denote the linear evolution operator over a time τ defined by Eqs. (2a) and (2b),

$$\mathbf{u}'(\tau) = \mathscr{A}(\tau)\mathbf{u}'(0).$$

Typically, the transient growth is defined with respect to the energy norm of the perturbation field, derived from the L_2 inner product

$$2E(\mathbf{u}') = (\mathbf{u}', \mathbf{u}') \equiv \int \mathbf{u}' \cdot \mathbf{u}' \, dv,$$

where E is the kinetic energy per unit mass of the perturbation, integrated over the spatial domain (dv). Since the governing equations are linear it is sufficient to consider the initial perturbation field $\mathbf{u}'(0)$ to have unit norm. The transient energy growth over interval τ is[28]

$$\frac{E(\tau)}{E(0)} = (\mathbf{u}'(\tau), \mathbf{u}'(\tau)).$$

In terms of the operator $\mathscr{A}(\tau)$ and its adjoint $\mathscr{A}^*(\tau)$ in the L_2 inner product,

$$\frac{E(\tau)}{E(0)} = (\mathscr{A}(\tau)\mathbf{u}'(0), \mathscr{A}(\tau)\mathbf{u}'(0))$$

$$= (\mathbf{u}'(0), \mathscr{A}^*(\tau)\mathscr{A}(\tau)\mathbf{u}'(0)),$$

where $\mathscr{A}^*(\tau)$ is obtained by integrating the adjoint linearized Navier–Stokes equations backwards over interval τ. The adjoint quasi-two-dimensional Navier–Stokes equations differ only slightly from the form derived in Ref. 42 due to the addition of the Hartmann friction term.

The adjoint equations are expressed as

$$\frac{\partial \mathbf{u}^*}{\partial t} = -DN^*\mathbf{u}^* - \nabla p^* + \frac{1}{Re}\nabla^2\mathbf{u}^* - 2\frac{d^2}{a^2}\frac{Ha}{Re}\mathbf{u}^*, \tag{3a}$$

$$\nabla \cdot \mathbf{u}^* = 0. \tag{3b}$$

Let λ_j and $\mathbf{v}_j$ denote eigenvalues and normalized eigenfunctions of the operator $\mathscr{A}^*(\tau)\mathscr{A}(\tau)$, then

$$\mathscr{A}^*(\tau)\mathscr{A}(\tau)\mathbf{v}_j = \lambda_j\mathbf{v}_j.$$

The maximum possible energy growth, denoted $G(\tau)$, over a specified time τ, is then given by the dominant eigenvalue of $\mathscr{A}^*(\tau)\mathscr{A}(\tau)$, i.e.,

$$G(\tau) = \max(\lambda_j).$$

The global maximum is denoted by

$$G_{\mathrm{max}} = \max(G(\tau)).$$

Aside from the additional Hartmann friction term in the forward and adjoint equations, the direct transient growth technique applied here is identical to that described in Ref. 27, and the linearized eigenmode solver employed here has been validated in Refs. 43 and 44. The equations are discretised in space using a spectral element approach.[45,46] The chosen scheme is further described in Ref. 10.

The boundary conditions are imposed on Eqs. (1a) and (1b) as follows. A no-slip boundary condition for velocity is imposed on all solid walls. At the channel inlet, a Hartmann velocity profile for the axial velocity is applied.[47] At the exit, a constant reference pressure is imposed and a zero streamwise gradient of velocity is weakly imposed through the Galerkin treatment of the diffusion term of the momentum equation. A high-order Neumann condition for the pressure gradient is imposed on the Dirichlet velocity boundaries to preserve the third-order time accuracy of the scheme.[48] During transient growth analysis, zero-velocity Dirichlet boundary conditions are imposed on the perturbation field on all boundaries during integration of the forward and adjoint equations.

The computational domain is divided into a grid of elements. Elements are concentrated in areas of the domain that experience high velocity gradients. The meshes comprise between 1052 and 1484 elements, depending on blockage ratio, and details of meshes can be found in Ref. 10. The upstream and downstream lengths x_u and x_d chosen for this study are 8 and 25, respectively, as determined by the domain size study below. The dependence of energy growth on upstream domain length is determined through the calculation of energy growth at a fixed time span of $\tau = 6$. Tables I and II show the effect of truncating the domain upstream length while keeping the downstream length and the inner portion of the mesh constant. For each blockage ratio, two Reynolds numbers are considered to ensure that the mesh chosen is adequate to resolve the solution in the subcritical range. For $\beta = 0.1$ and $Ha^* = 50$, $Re = 200$ and 580 are considered, and for $\beta = 0.4$ and $Ha^* = 50$, $Re = 400$ and 1160 are considered. It can be noted that the effect of truncating the upstream length from $32d$ to $8d$ results in less than a 3% difference in the growth rate prediction for the four cases in

TABLE I. The effect of variation of upstream domain length on growth energy at $\tau = 6$ across blockage $\beta = 0.1$ for $Ha^* = 50$ for different Reynolds numbers as indicated.

x_u	$\beta = 0.1, Re = 200$		$\beta = 0.1, Re = 580$	
	$G(6)$	% Error	$G(6)$	% Error
4	8.9665×10^{-2}	5.912	1.4353×10^3	21.6
8	8.5021×10^{-2}	0.427	1.2150×10^3	2.93
16	8.4665×10^{-2}	0.0065	1.1858×10^3	0.469
32	8.4660×10^{-2}	0.0000	1.1803×10^3	0.000

TABLE II. The effect of variation of upstream domain length on growth energy at $\tau = 6$ across blockage $\beta = 0.4$ for $Ha^\star = 50$ and different Reynolds numbers as indicated.

| x_u | $\beta = 0.4$, $Re = 400$ | | $\beta = 0.4$, $Re = 1160$ | |
	$G(6)$	% Error	$G(6)$	% Error
4	6.4643×10^{-4}	0.145	3.3138×10^{4}	0.606
8	6.4737×10^{-4}	0.0004	3.3140×10^{4}	0.599
16	6.4737×10^{-4}	0.0000	3.3313×10^{4}	0.0825
32	6.4737×10^{-4}	0.0000	3.3340×10^{4}	0.0000

Tables I and II. As might be expected higher Reynolds number increases the error, while increasing the Hartmann number decreases the error.

A grid resolution study was undertaken to determine a suitability accurate element polynomial degree. The polynomial degree used for most simulations was $N_p = 7$. Convergence tests were performed on two cases, chosen at the upper end of the parameter range of this study. The first case featured $\beta = 0.1$, $Ha^\star = 120$, and $Re = 1000$, and the second featured $\beta = 0.4$, $Ha^\star = 480$, and $Re = 2000$. The results of these tests are shown in Table III, which shows convergence of the normalized length of the recirculation zone behind the cylinder (measured downstream from the aft surface of the cylinder), and the growth rate of the leading eigenmode from a linear stability analysis.[44,49]

The present transient growth analysis implementation is validated firstly for a non-magnetohydrodynamic flow. The flow past a circular cylinder in an open flow at sub and supercritical Reynolds numbers $Re = 45$ and 50 is considered for this test case, which was investigated recently by Ref. 35. A comparison between the results of the present solver and the previous study is shown in Fig. 2.

The respective structure and the evolution of the optimal disturbance field at $Re = 50$ are shown in Figs. 2(b)–2(e). In Fig. 2(b), the vorticity of the base flow around the circular cylinder at this Reynolds number is shown. Figure 2(c) shows the initial perturbation associated with a time interval $\tau = 32$. It is observed that the optimal disturbance structures are concentrated around the region of the boundary layer separation in the near wake. In Fig. 2(d), the evolution from this optimal initial disturbance to time $t = 32$ is shown. The optimal disturbance is shown to evolve to a flow structure comprising a series of counter-rotating spanwise rollers. The disturbance structures reproduced from Ref. 35 are virtually indistinguishable from those computed using our implementation. This, in addition to the excellent agreement found for predicted energy growths (G) in Fig. 2(a), verifies that our implementation is performing correctly.

Finally, a check of the transient growth analysis implementation incorporating the Hartmann friction term is performed. For $\beta = 0.1$, $Ha^\star = 50$, and $Re = 580$, the predicted optimal initial disturbances were evolved using the linearized quasi-two-dimensional Navier–Stokes solver, and energy time histories normalized by the initial energy were recorded. Correct performance of the transient growth solver is confirmed by the normalized energy time histories agreeing with the corresponding predicted energy growth factors (G). Of course, since the transient growth solver

TABLE III. Convergence of the normalized circulation length L_R/d and maximum growth rate σ across blockage ratio $\beta = 0.1$, $Ha^\star = 120$ and $\beta = 0.4$, $Ha^\star = 480$ with increasing polynomial order.

| N_p | $\beta = 0.1$, $Re = 1000$ | | $\beta = 0.4$, $Re = 2000$ | |
	L_R/d	σ	L_R/d	σ
5	1.511	-0.04991	0.721	-0.1053
6	1.552	-0.07281	0.724	-0.1287
7	1.549	-0.09185	0.725	-0.1572
8	1.526	-0.09122	0.725	-0.1579
9	1.532	-0.09136	0.725	-0.1584
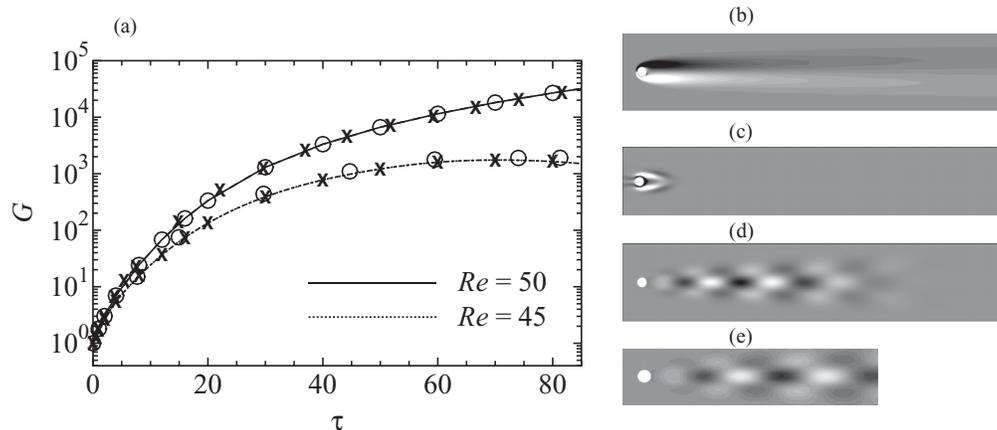
FIG. 2. (a) Predicted energy growth (G) plotted against τ, for the flow past a circular cylinder in an open flow at $Re = 45$ and $Re = 50$ without a magnetic field. Results using the present solver ($\bigcirc$) and data from Ref. 35 ($\times$) are shown. The solid and dashed curves show a spline fit to the present data for guidance. (b)–(e) Contours of vorticity plotted at $Re = 50$ for the case without magnetic field. (b) The two-dimensional base flow. (c) The predicted optimal initial condition. (d) The evolution of the optimal disturbance at time $t = \tau = 32$. (e) The corresponding result at $\tau = 32$ and $Re = 50$ reprinted from Abdessemed et al.[35] [Physics of Fluids **21**, 044103 (2009)]. Copyright 2009, American Institute of Physics. Contour levels over $|\omega| \leq 1$ and $|\omega| \leq 0.01$ are plotted in (a) and (b), respectively.

depends on the linearized two-dimensional Navier–Stokes solver, this test only validates the former implementation relative to the latter.

Having validated the transient growth solver, this study now proceeds to investigate the transient response of liquid metal flows in an electrically insulated rectangular duct past a circular cylinder under a strong axial magnetic field in the subcritical regime below the onset of von Kármán vortex shedding. Consideration is given to parameters over the ranges $50 \leq Re \leq 2050$, $50 \leq Ha^\star \lesssim 500$, and $0.1 \leq \beta \leq 0.4$.

III. RESULTS: WAKE STRUCTURE AND SCALING

The base flow is characterized by a pair of symmetric counter-rotating vortices on either side of the wake centerline, immediately behind the cylinder. Figure 3 shows isocontours of the stream function (streamlines) at $Re = 580$ and different blockage ratios and Hartmann numbers. It can be seen that an increase in the Hartmann number acts on the wake by decreasing the length of the recirculation bubble. This is due to the dominance of the Lorentz forces which results in a damping in a direction opposite the flow, resulting in the decrease of the wake length. Similarly, increasing the blockage ratio was also found to decrease the wake length. For $\beta = 0.1$, the recirculation bubble
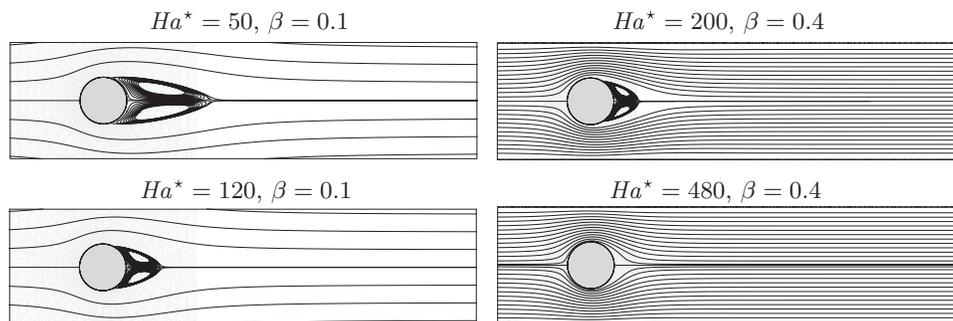
FIG. 3. Streamlines of the steady base flows at $Re = 580$, blockage ratios $\beta = 0.1$ (left) and 0.4 (right), and Hartmann numbers as indicated. Flow is left to right in each frame.

clearly still exists at $Ha^\star = 120$. At $\beta = 0.4$, additional computations (not shown) determined that it was suppressed completely beyond $Ha^\star \gtrsim 300$.

The length of the wake is of particular interest when considering the behavior of transient disturbances in the flow, as recent studies have shown that separated shear layers (such as those bordering the wake behind the cylinder in the present study) are particularly sensitive to transient disturbances.[27,29,42] Here, then, increasing the Reynolds number broadly acts to increase the wake length, while increasing the modified Hartmann number acts to decrease the wake length. Increasing the blockage ratio is found to only weakly act to increase the wake length. To quantify these observations, the wake length (L_R/d, taken as the distance from the aft surface of the cylinder to the stagnation point defining the end of the recirculation bubble) was recorded at a large number of points in the Re–$Ha^\star$–β parameter space. For a single β, L_R/d increases almost linearly with increasing Re for a constant $Ha^\star$, and decreases with $Ha^\star$ for a constant Re. Reference 9 proposed for $\beta = 0.25$ that L_R/d data collapsed onto a universal curve when plotted against $Re/Ha^{0.8}$, but in this study a more general universal relationship is sought that also incorporates the blockage ratio. A non-linear optimization was conducted to find exponents A, B, and C accurate to three significant figures that serve to maximize the square of the correlation coefficient (r^2) of a linear least-squares fit to the L_R/d data when plotted against $Re^A Ha^{\star B} \beta^C$. The optimal exponents were determined to be $A = 0.844$, $B = -0.711$, and $C = 0.166$. The universal relationship between recirculation length, Reynolds number, Hartmann number, and blockage ratio over ranges of modified Hartmann number $50 \leq Ha^\star \lesssim 500$, Reynolds number $50 \leq Re \leq 2050$, and blockage ratios $0.1 \leq \beta \leq 0.4$ is thus approximated by

$$L_R/d = 0.282\left(Re^{0.844} Ha^{\star -0.711} \beta^{0.166}\right) - 0.709, \tag{4}$$

and the pleasing collapse of the data obtained as a result of this analysis is shown in Fig. 4.

Equation (4) can be used to estimate at which values of the parameters the separation bubble will first appear (i.e., by solving for $L_R/d = 0$). This gives

$$Re = 2.983\, Ha^{\star 0.842} \beta^{-0.197}.$$

For the bookend blockage ratios considered in this study ($\beta = 0.1$ and 0.4), the separation bubble threshold is defined by

$$Re = 4.692\, Ha^{\star 0.842} \tag{5}$$

and

$$Re = 3.572\, Ha^{\star 0.842}, \tag{6}$$
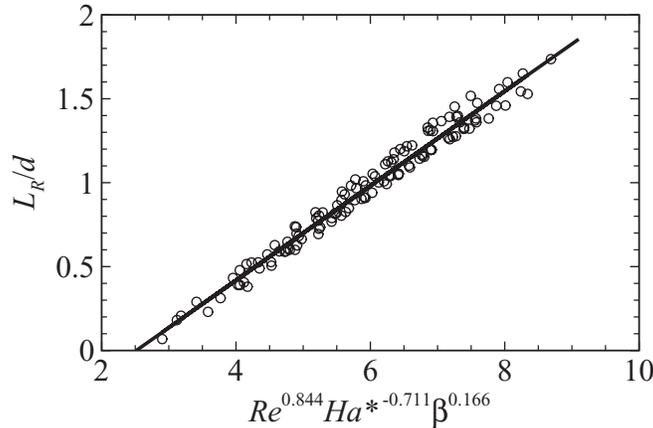
FIG. 4. Collapse of recirculation zone lengths over ranges of modified Hartmann numbers $50 \leq Ha^\star \lesssim 500$, Reynolds numbers $50 \leq Re \leq 2050$, and blockage ratios $0.1 \leq \beta \leq 0.4$ when plotted against ($Re^{0.844} Ha^{\star -0.711} \beta^{0.166}$).

respectively. To illustrate the application of these relationships, Fig. 3 plots flow streamlines at several combinations of $Ha^\star$ and β, and a constant Reynolds number $Re = 580$. For $\beta = 0.1$, Eq. (5) estimates critical Reynolds numbers of $Re = 127$ at $Ha^\star = 50$ and $Re = 265$ for $Ha^\star = 120$. The plotted Reynolds number exceeds both of these critical Reynolds numbers, and therefore for both of these cases a wake recirculation bubble would be expected. The plots in the first two frames of Fig. 3 confirm this. For $\beta = 0.4$, Eq. (6) estimates critical Reynolds numbers of $Re = 310$ (less than $Re = 580$) at $Ha^\star = 200$ and $Re = 648$ (greater than $Re = 580$) at $Ha^\star = 480$. Hence, a wake recirculation bubble is expected to be observed in the former case but not the latter, which is consistent with observation of the results in Fig. 3. For the first three cases shown in Fig. 3 that produce wake recirculation bubbles, the wake lengths estimated by Eq. (4) are $L_R/d = 1.85, 0.665$, and 0.494, respectively, which compare well with the wakes seen in the figure.

IV. RESULTS: TRANSIENT ENERGY GROWTH

Firstly, the results as a function of τ and $Ha^\star$ for a fixed value of Re at different blockage ratios β are presented, and subsequently the dependence on Re is considered.

A. Hartmann number dependence on optimal growth

Figure 5 shows the transient energy growth G of optimal disturbances as a function of time interval τ for the steady base flow at four different blockage ratios over $0.1 \leq \beta \leq 0.4$ at different Hartmann numbers and $Re = 400$. The initial observation on these data is, though the chosen Re for the analysis is well below the critical Reynolds number for unsteady flow at the lowest Hartmann number $Ha^\star = 50$, there exist perturbations which grow in energy by sometimes more than a thousand times. In addition, the significant damping effect of Hartmann number is also revealed. For example, for $\beta = 0.1$ the peak energy growth is 60.93 and 2.72 at $Ha^\star = 50$ and $Ha^\star = 120$, respectively. For $\beta = 0.4$, there is growth of energy by a factor of 1.86×10^3 and 7.22×10^3, respectively. For all β, it is found that increasing $Ha^\star$ leads to a significant reduction of the energy amplification of the
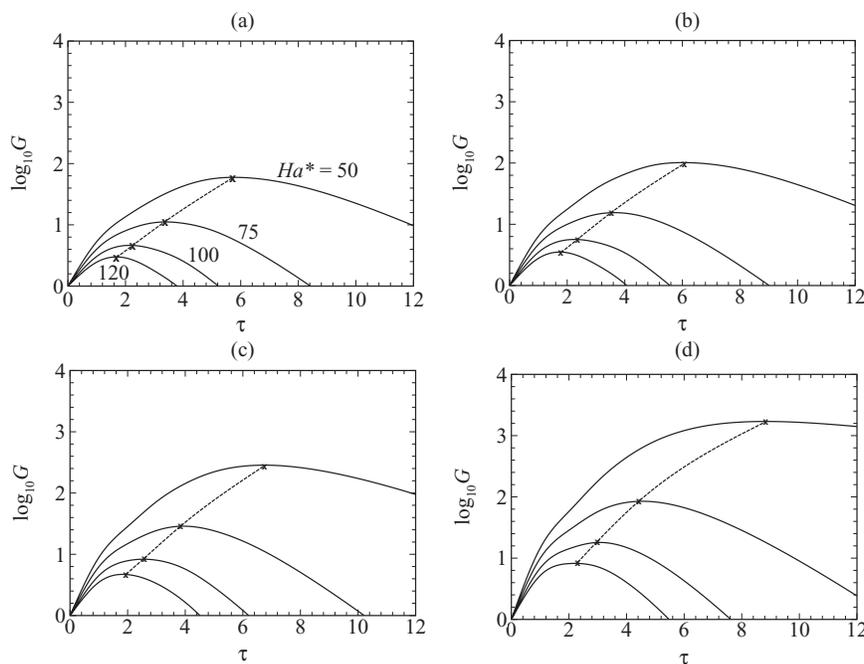
FIG. 5. Plots of $\log_{10} G$ against τ, at blockage ratio and Hartmann numbers as shown for $Re = 400$. The dashed-line curve shows the locus of maximum growth as a function of τ. (a) $\beta = 0.1$; (b) $\beta = 0.2$; (c) $\beta = 0.3$; and (d) $\beta = 0.4$.

disturbances and to a shift of the peak growth towards smaller times. This is not surprising given that the Hartmann term acts as an extra damping in addition to viscous damping. However, for a fixed modified Hartmann number, the global maxima of energy growth also varies significantly with blockage ratio, being larger at higher β, and the maximum amplification occurs for larger times. This is probably a result of the increased acceleration of the flow in the neighborhood of the cylinder for higher blockage ratios, making the Reynolds number effectively higher for higher β, although increasing β also shortens the separation bubble length as well.

B. Structure and evolution of optimal disturbance fields

Figure 6 plots the vorticity field of the optimal initial perturbations for the four blockages considered in this study (as presented in Fig. 5) at modified Hartmann numbers $Ha^\star = 50$ and 120. In each, the optimal disturbance field is localized in the region of the boundary layer separation around the cylinder near the wake as also observed in the analysis of Refs. 32, 50, and 51 for the case without a magnetic field ($Ha = 0$). The structure of the disturbance near the separation bubble is consistent across these blockage ratios; however, at the higher blockage ratios the optimal field does not drop away to zero towards the side boundaries. This contributes to subsequent downstream amplification, as will be demonstrated in later plots. The perturbation initially convects along the separating region being amplified to the peak growth state downstream of the recirculation bubble. In Fig. 7, the resulting time interval for maximum growth, τ_{max}, is plotted as a function of the circulation length at $Ha^\star = 50$. It is observed that τ_{max} increases significantly as circulation length increases. This is commensurate with the amplifying nature of the separated shear layers in the wake, as the disturbance travels further and grows larger as it convects down the longer wake. This phenomenon is consistent with transient growth in several systems, including a plane channel,[24] rectangular duct,[25] and abrupt geometrical expansion flows.[27–30]
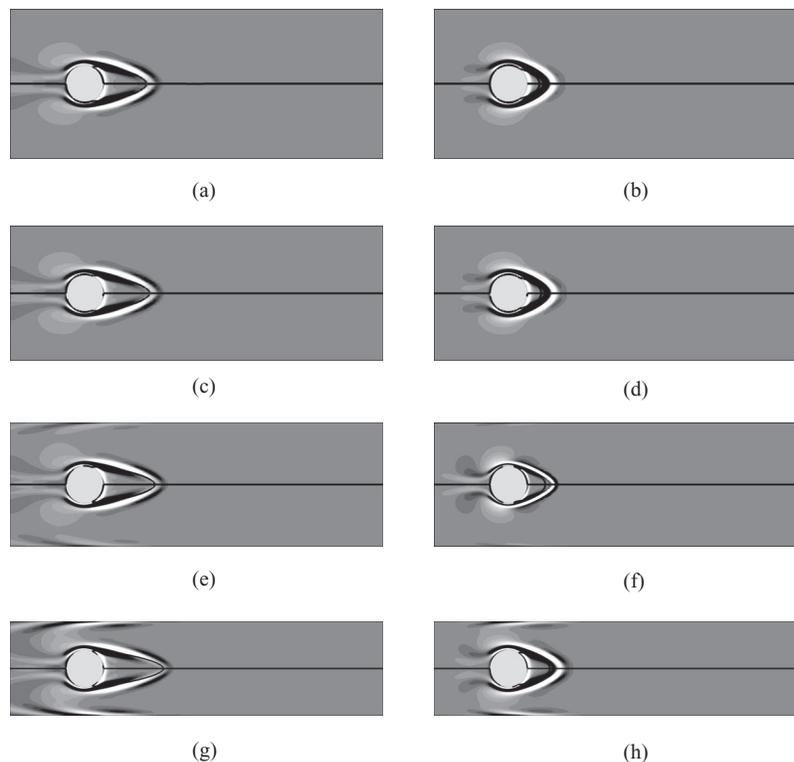
FIG. 6. Plots of vorticity of the optimal initial perturbation at τ_{max} and blockage ratios as labeled for $Re = 400$. Modified Hartmann numbers $Ha^\star = 50$ (left) and 120 (right) are shown. The streamlines of the stable base flow are overlaid in each case. (a) and (b) $\beta = 0.1$; (c) and (d) $\beta = 0.2$; (e) and (f) $\beta = 0.3$; and (g) and (h) $\beta = 0.4$.
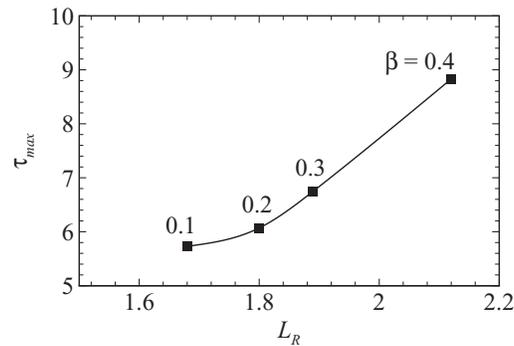
FIG. 7. Maximum τ of the energy maxima at $Ha^\star = 50$ and $Re = 400$ as a function of circulation length at different blockage ratios.
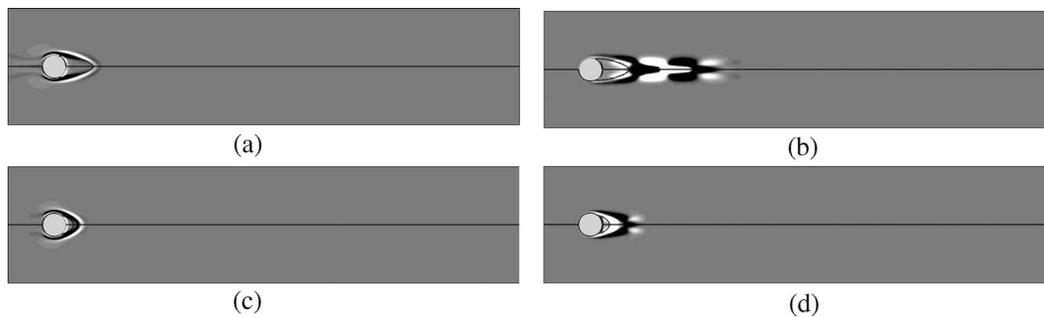
FIG. 8. Contours of vorticity for $\beta = 0.1$ and $Re = 400$. (a) and (c) show the optimal disturbance initial condition at $Ha^\star = 50$ and 120, respectively. (b) and (d) show the development of these linear disturbances to $t = \tau_{max} = 5.54$ and 1.72, respectively. Streamlines of the stable base flow are overlaid in each case. Vorticity contour levels of $|\omega| \leq 0.05$ are plotted in frames (a) and (c), and levels of $|\omega| \leq 0.5$ are plotted in frames (b) and (d).
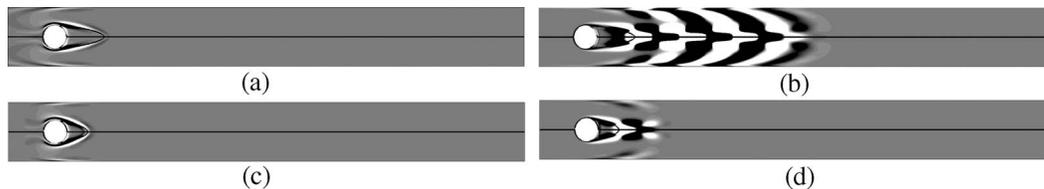
FIG. 9. Contours of vorticity for $\beta = 0.4$ and $Re = 400$. (a) and (c) show the optimal disturbance initial condition at $Ha^\star = 50$ and 120, respectively. (b) and (d) show the development of these linear disturbances to $t = \tau_{max}$. Contour levels are as per Fig. 8.

Figures 8(a) and 8(c) show the vorticity of the initial perturbation for $\beta = 0.1$ at $Re = 400$, and $Ha^\star = 50$ and 120, for which $\tau_{max} = 5.54$ and 1.72, respectively. It can be seen that independent of Hartmann number, the optimal perturbations remain concentrated around the limiting streamline identifying the recirculation bubble.

In Figs. 8(b) and 8(d), the evolution from this optimal initial disturbance is plotted, i.e., the disturbance that linearly evolves from these disturbances at $t = 5.54$ and $t = 1.72$. At the peak growth time, the disturbance flow structures present as a series of counter-rotating spanwise rollers. However, for $\beta = 0.4$, at $Ha^\star = 50$ (see Fig. 9(b)), interaction with the channel wall boundary layers (the Shercliff layers) occurs downstream of the cylinder. Vorticity is drawn into the channel and interacts with the vorticity detached from the rear of the cylinder. The level of wall boundary layer disturbance was observed to increase significantly as the blockage ratio increased from $\beta = 0.1$ to 0.4. In fact, for $\beta \lesssim 0.2$ there were no strong perturbation structures observed along the walls.
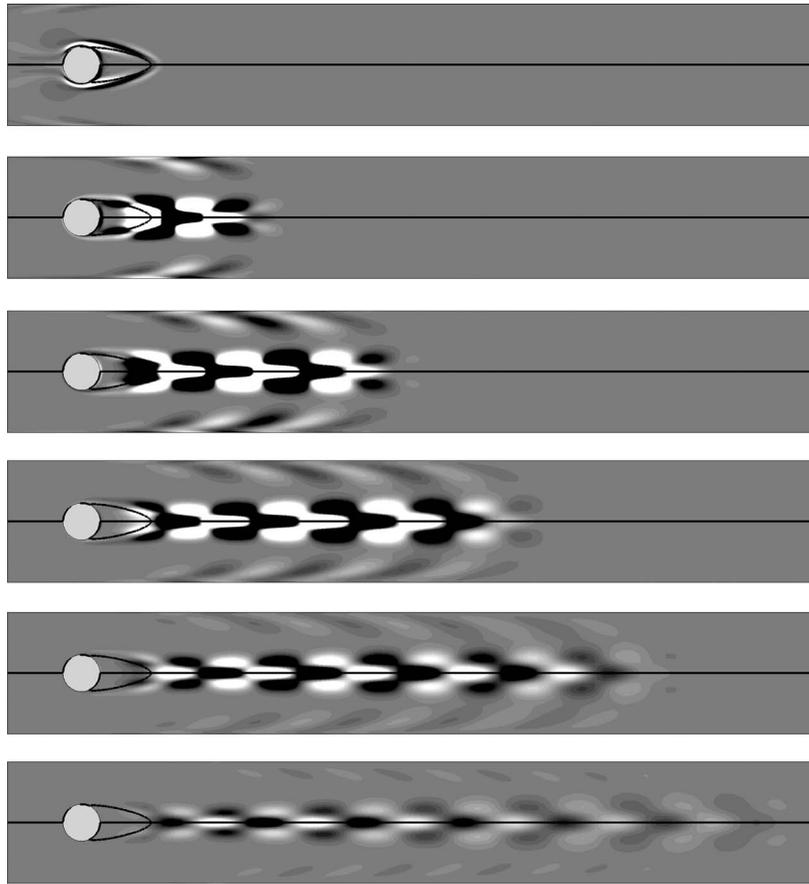
FIG. 10. Time sequence of linear perturbation vorticity contours developed from the optimal disturbance initial condition for $\beta = 0.3$, $Re = 400$, and $Ha^\star = 50$ at $t = \tau_{\max}$. Flow from left to right. From top to bottom, frames show times $t = 0, 4, 8$, 12, 16, and 20. White and black representing positive and negative vorticity, respectively. Separation streamlines of the base flow are overlaid in each case.

Consideration is now given to the time evolution of a predicted optimal disturbance from its initial condition, through to, and beyond, $\tau_{\max}$. Figure 10 shows a sequence of perturbation vorticity contours that evolve from the optimal initial state at $\beta = 0.3$, $Re = 400$, $Ha^\star = 50$, and $\tau = 6.90$. At early times, the disturbance that passes through this region interacts with the boundary layer (the Shercliff layers) detached from the walls. Then, the wave packet is amplified while traveling downstream. The disturbances consist of a roller packet structure and the maximum rate of growth occurs at the beginning of the sequence when the perturbation passes through the separation bubble. This spatial pattern indicates that the energetic amplification of the perturbation is, at least initially, analogous with convective instability: the amplitude of maximum energy growth moves in a frame convecting with the disturbance, and the energy at the initial disturbance location and downstream decays as the disturbance convects away.

To illustrate this, Fig. 11 shows the profiles of the vertical velocity component that evolve from the optimal initial state for the case shown in Fig. 10. The vertical velocity component is extracted along the line $y = 0$. The profiles are normalized to have absolute maximum value of unity. Again the characteristic dynamics of convective instability are suggested. The initial disturbance decays as the disturbance convects away. The extremely sharp fluctuation in the optimal perturbation can be observed in the boundary layer separation near the wake. The average streamwise wavelength of the fluctuations of the vortical structures leaving the circulation bubble at the optimal time estimated by zero-crossing analysis is $\lambda_x/d = 2.30$ and 2.59, at $Ha^\star = 50$ and 120, respectively. The characteristics
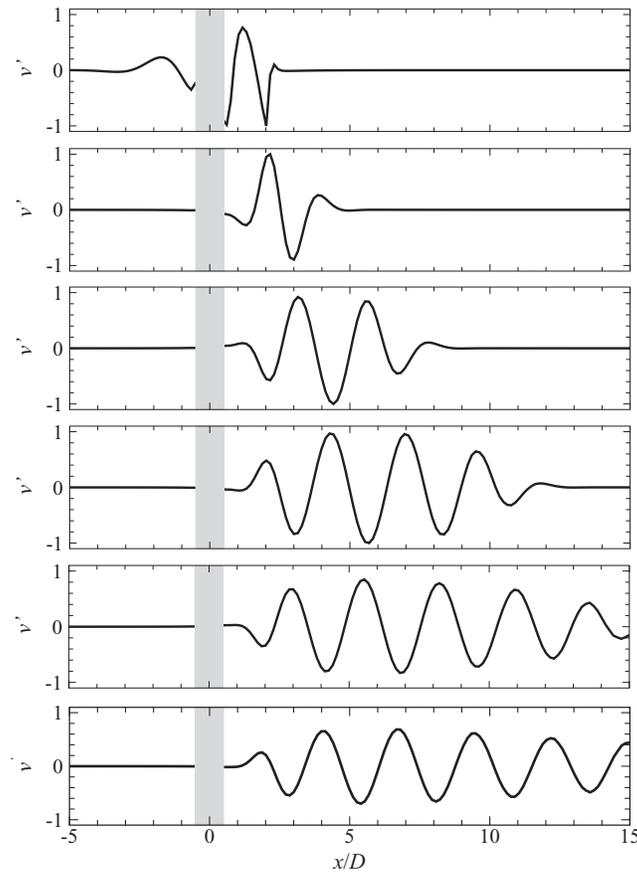
FIG. 11. Time sequence of the vertical component of the perturbation velocity (v') profile along the channel centerline obtained at $\beta = 0.3$, $Re = 400$, and $Ha^\star = 50$. The sequence evolves from the optimal disturbance achieving peak energy growth, which had an evolution time $\tau_{max} = 6.90$. From top to bottom, frames show times $t = 0, 4, 8, 12, 16$, and 20. The shaded region denotes the location of the cylinder.

of the optimal perturbation fields at the point of maximum growth for the case of $Ha^\star = 50$ and 120 at different blockage ratios are given in Table IV.

Figure 12 presents a sequence of the base-10 logarithm of energy contours that evolved from the initial optimal disturbance obtained at $\beta = 0.3$, $Re = 1075$, $Ha^\star = 150$, and $\tau = 7.51$. The flow structures that give rise to these energy contours are a series of counter-rotating spanwise rollers. Initially, the energies of the optimal disturbance are concentrated around the cylinder. Then, the disturbance energy convects downstream along the separated shear layer and is amplified until $t = \tau_{max}$. For $t > \tau_{max}$, there is no significant further downstream convection of the disturbance,

TABLE IV. Characteristics of the optimal perturbations at the time of maximum growth τ_{max} for different blockage ratios at Hartmann numbers as indicated and a Reynolds number $Re = 400$. Along with τ_{max} the centroid location x_c of the evolved perturbation energy, the local axial wave length λ_x, and the frequency f of the perturbation.

β	$Ha^\star = 50$				$Ha^\star = 120$			
	x_c	τ_{max}	λ_x	f	x_c	τ_{max}	λ_x	f
0.1	2.57	5.54	2.54	0.3	1.60	1.72	1.81	0.25
0.2	3.10	6.10	2.37	0.32	1.18	1.83	2.37	0.27
0.3	4.00	6.90	2.30	0.36	1.37	2.01	2.59	0.28
0.4	4.67	8.26	2.21	0.4	1.75	2.43	2.89	0.35
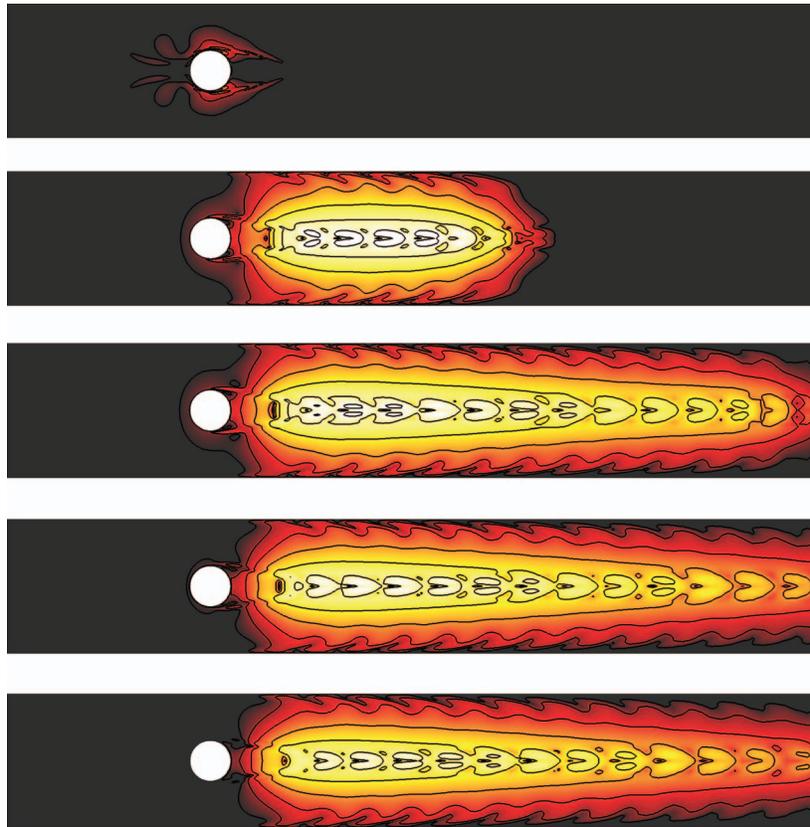
FIG. 12. (Color online) Contours of the base-10 logarithm of energy developed from the global optimum disturbance initial condition for $\beta = 0.3$, $Re = 1075$, and $Ha^\star = 150$. From top to bottom, frames show times $t = 0, 4, 8, 16$, and 32.

which instead remains largely in place several diameters downstream of the cylinder, where it slowly decays away. The centroid location of the energy of the global linear instability mode (a real eigenmode computed from a linear stability analysis corresponding to a growth rate $\sigma = -0.0402$) lies at $x_c \approx 3.5$. For the optimal disturbance at $t = \tau_{\max}$ and $t > \tau_{\max}$, the centroid location of evolved perturbation energy are $x_c = 4.22$ and $x_c \approx 3.5$, respectively. These properties imply that the action of the optimal disturbance is to perturb the leading global instability mode. This behavior is consistent with the observation for a circular cylinder in a non-magnetohydrodynamic flow.[35]

C. Reynolds number dependence

The Reynolds number dependence of the maximum growth and the associated disturbances are now considered. Figure 13 shows the predicted transient energy growth G of optimal perturbations as a function of evolution time τ for the steady base flows. For all β, while the chosen Reynolds numbers for the analysis are well below Re_c, there exist perturbations that grow in energy by factors of 3.81×10^2, 6.99×10^2, 2.0×10^3, and 1.89×10^4 at $\beta = 0.1, 0.2, 0.3$, and 0.4, respectively. For all Re at $Ha^\star = 120$, it is found that increasing β leads to a significant increase of the energy amplification and to a shift of the global maxima towards larger evolution times. For $\beta \leq 0.3$, there is a substantial change in the $\tau_{\max}$ of the global maxima. However, this is less pronounced for $\beta \gtrsim 0.2$, where $\tau_{\max}$ occurs consistently at smaller τ.

The critical Reynolds number for positive energy growth of optimal disturbances, Re_{c1}, corresponds to the Reynolds number below which $G(\tau) \leq 1$ for all τ. By inspection of this data, this corresponds to the Reynolds number at which the gradient of G–τ data at $\tau = 0$ is zero, as for smaller Re, G decreases monotonically with τ. For each β, gradients were obtained for each Reynolds
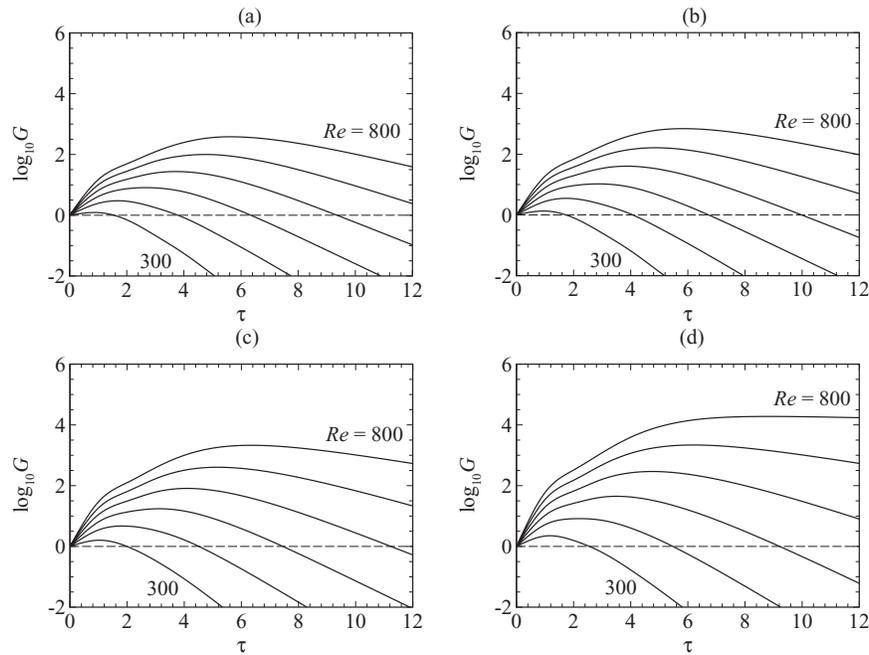
FIG. 13. Plots of the transient energy growth, G, against τ, at different blockage ratio for Reynolds numbers from 300 to 800. (a) $\beta = 0.1$, $Ha^* = 120$, (b) $\beta = 0.2$; $Ha^* = 120$; (c) $\beta = 0.3$, $Ha^* = 120$; and (d) $\beta = 0.4$, $Ha^* = 120$.

number using polynomial curve fitting. The resulting Re_{c1} at $Ha^\star = 50$ and 120 for different blockage ratios are presented in Table V. These results demonstrate that it is possible to find disturbances which invoke positive energy growth around a circular cylinder. For all β (see Fig. 13), it can be seen that for $Re \geq Re_{c1}$ the optimal curve has a positive slope at $\tau = 0$ and there is a range of τ for which the energy of an optimal disturbance increases rather than decreases from its initial value.

Figures 14(a) and 14(b) and 15(a) and 15(b) show the variations of $\log_{10} G_{max}$ and τ_{max} as functions of Re for different β at $Ha^\star = 50$ and 120, respectively. For all β, it is found that G_{max} grows exponentially or faster with Re at $Ha^\star = 50$ and 120. For low Hartmann numbers the growth appears to be quadratic with Re, at least initially beyond the onset of positive amplification (though it is noted that only 4 data points are used to determine each trend). At higher Reynolds numbers and at higher Hartmann numbers (e.g., Fig. 15) the variation appears to be linear. This is consistent with previous findings for non-magnetic bluff body flows.[27] At the higher Hartmann number the growth is much closer to linear from the point of positive amplification. In addition, for a given β, there is a significant change in the asymptotic slope of the curves as Hartmann number increases from $Ha^\star = 50$ to 120, decreasing by almost 40%. Furthermore, G_{max} at $Ha^\star = 50$ increases by a factor of approximately 8.13, 9.12, 14.7, and 33.1, and 3.72, 4.17, 5.01, and 7.76 for $Ha^\star = 120$ for each Re increment of 100, for $\beta = 0.1$, 0.2, 0.3, and 0.4, respectively.

TABLE V. Critical Reynolds numbers for positive energy growth of optimal disturbances Re_{c1} for $Ha^\star = 50$ and 120 as indicated for different blockage ratios.

β	Re_{c1} ($Ha^\star = 50$)	Re_{c1} ($Ha^\star = 120$)
0.1	248.53	283.43
0.2	164.49	275.78
0.3	157.46	263.37
0.4	140.69	241.55
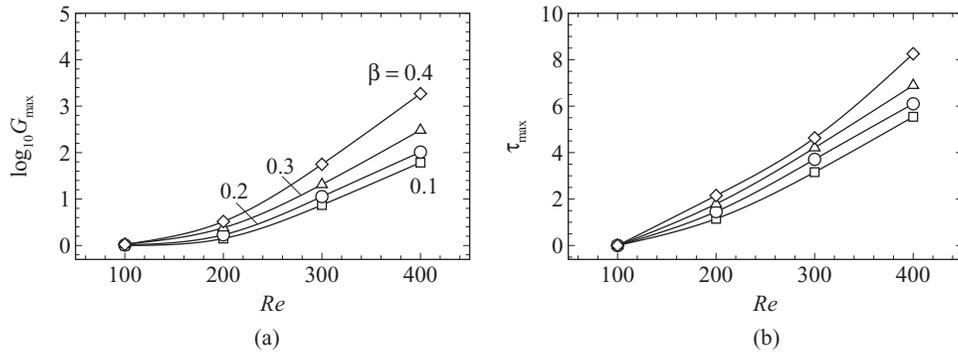
FIG. 14. Maximum energy growth G_{max} (a) and time of maximum of the energy maximum (b) as a function of Reynolds number for different blockage ratios β at $Ha^\star = 50$. Linear trends in the data in (a) signify an exponential relationship. The values of Re displayed are below the critical Reynolds numbers for global instability. The asymptotic slopes of $\partial \log_{10} G_{max}/\partial Re$ at $\beta = 0.1, 0.2, 0.3$, and 0.4 are $0.0091, 0.0096, 0.0117$, and 0.0152, respectively.

For larger Reynolds numbers, a linear variation between τ_{max} and Re is observed, corresponding to the higher-Reynolds-number linear regime observed for $\log G_{max}$. The slopes of these trends only display a very weak blockage ratio dependence compared to the G_{max} variation.

V. RESPONSE OF THE FLOW TO CONTINUOUS UPSTREAM DISTURBANCES

To demonstrate the relevance of linear growth computations to a real flow in the presence of inflow noise, direct numerical simulations have been performed. The initial state is the steady flow at $Re = 1160$, $Ha^\star = 200$, and $\beta = 0.4$. This case has been chosen as it exhibits the maximum energy growth of all the cases investigated in Sec. IV. For this purpose a random white noise with small amplitude is added to the velocity field at the inlet to the computational domain. Therefore, we aim to see strong evidence of disturbances growing to non-linear levels as the base flow is excited with noise. Of course, inflow noise represents a continuous forcing while the transient growth analysis examines the growth of discrete wavepackets, so some care make be taken with the interpretation of the results.

In a non-magnetohydrodynamic flow, an injected disturbance decays only through the action of viscosity. However, in these flows Hartmann damping also acts to damp disturbances. The rate at which disturbance vorticity (ω) decays can be approximated using Eq. (15) in Ref. 10. Using this expression for these flow conditions gives $\frac{d(\log_e \omega)}{dt} \approx -0.344$. If it is assumed that inflow disturbances convect at approximately U_0, then by the time a disturbance reaches the cylinder,
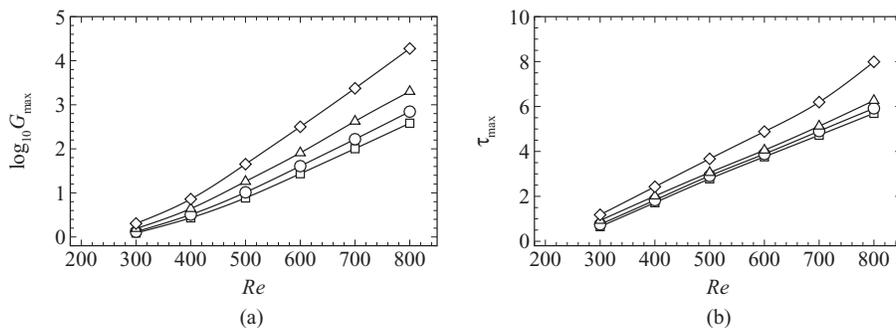
FIG. 15. Maximum energy growth G_{max} (a) and time of maximum of the energy maximum (b) as a function of Reynolds number for different blockage ratios β at $Ha^\star = 120$. The values of Re displayed are again below the critical Reynolds numbers. The asymptotic slopes of $\partial \log_{10} G_{max}/\partial Re$ at $\beta = 0.1, 0.2, 0.3$, and 0.4 are $0.0057, 0.0062, 0.007$, and 0.0089 respectively. Symbols as per Fig. 14.
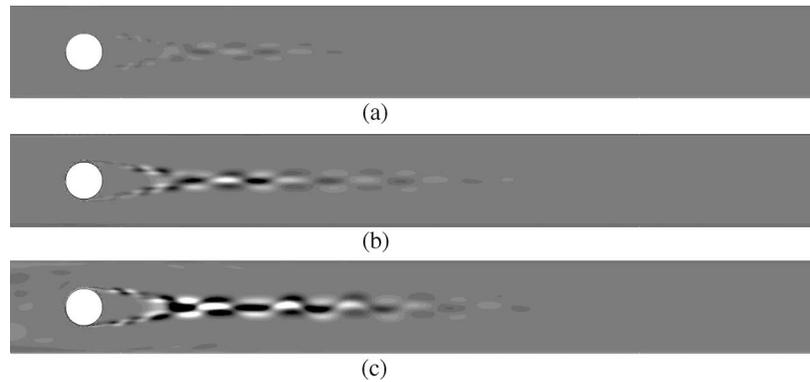
FIG. 16. Disturbance vorticity contours obtained for $Re = 1160$, $Ha^{\star} = 200$, and $\beta = 0.4$. The disturbance velocity field was isolated by subtracting the unperturbed steady-state solution from a snapshot of the simulations perturbed by white noise. Shown are cases computed with envelopes of white noise amplitudes of (a) $0.1U_0$, (b) $0.3U_0$, and (c) $0.5U_0$.

it will have decayed to just 7.5% of its original strength. This Hartmann damping would be even stronger at lower Reynolds numbers and higher Hartmann numbers. Ultimately, this means that upstream disturbances need to be significantly stronger in these magnetohydrodynamic flows than in comparable non-magnetohydrodynamic channel flows to facilitate amplification of the disturbances to non-linear levels.

Figure 16 shows the vorticity in the disturbance invoked by the addition of white noise to the inflow. Even for low levels of random noise (e.g., a disturbance envelope of $0.1U_0$), a distinct pattern of disturbance is observed behind the cylinder. This disturbance pattern appears in the vicinity of the separation of the flow from the sides of the cylinder, and is observed to propagate downstream along the separated shear layers in the wake, becoming broader. These flaring disturbance zones meet at the wake centerline, and further downstream a disturbance pattern is observed which is consistent with those observed to have evolved from the optimal initial disturbance leading to maximum energy growth for the given parameters.

Further analysis of the system with the inflow perturbed by white noise with an amplitude of $0.5U_0$ is elucidated in Fig. 17. In Fig. 17(a), a simulated dye visualization image is produced[45,52] following injection of a high concentration of passive tracer particles into the flow from the vicinity of the surface of the cylinder. Particles are evolved using an implementation[53] of the high-order particle transport algorithm of Coppola *et al.*[54] This visualization approach reveals an instantaneous streakline pattern in the flow, which demonstrates that at these flow and perturbation conditions (which are below the critical Reynolds number for the onset of vortex shedding), the level of upstream disturbance is sufficient to invoke an observable wavy disturbance downstream of the wake recirculation bubble.

Figure 17(b) plots vorticity in the flow, which exhibits the same wavy perturbation seen in Fig. 17(a). The flow is characterized by a pair of symmetric counter-rotating vortices on either side of the wake centerline. The bubble length of the wake is of particular interest when considering the behavior of transient disturbances in the flow, as separated shear layers appear to consistently act as an amplifier of disturbances. Note that the vorticity decays relatively quickly downstream of the wake recirculation bubble due to Hartmann damping, though waviness in the dye streak persists further downstream. This may have significant implications for efforts to enhance mixing across magnetohydrodynamic channel flows.

Attention is now directed to the disturbance field, which is generated by subtracting the unperturbed flow from the perturbed flow. In Fig. 17(c), vorticity in the disturbance field is plotted. In comparison to the strength of vorticity structures in the wake, very weak vorticity structures can be observed to the left of the cylinder. This demonstrates the significant degree by which disturbances have been amplified as they convect past and downstream of the cylinder. Included for comparison with this disturbance field are the corresponding optimal perturbation evolved to τ_{max} and the leading global linear instability mode (Figs. 17(f) and 17(g), respectively). Downstream of the recirculation
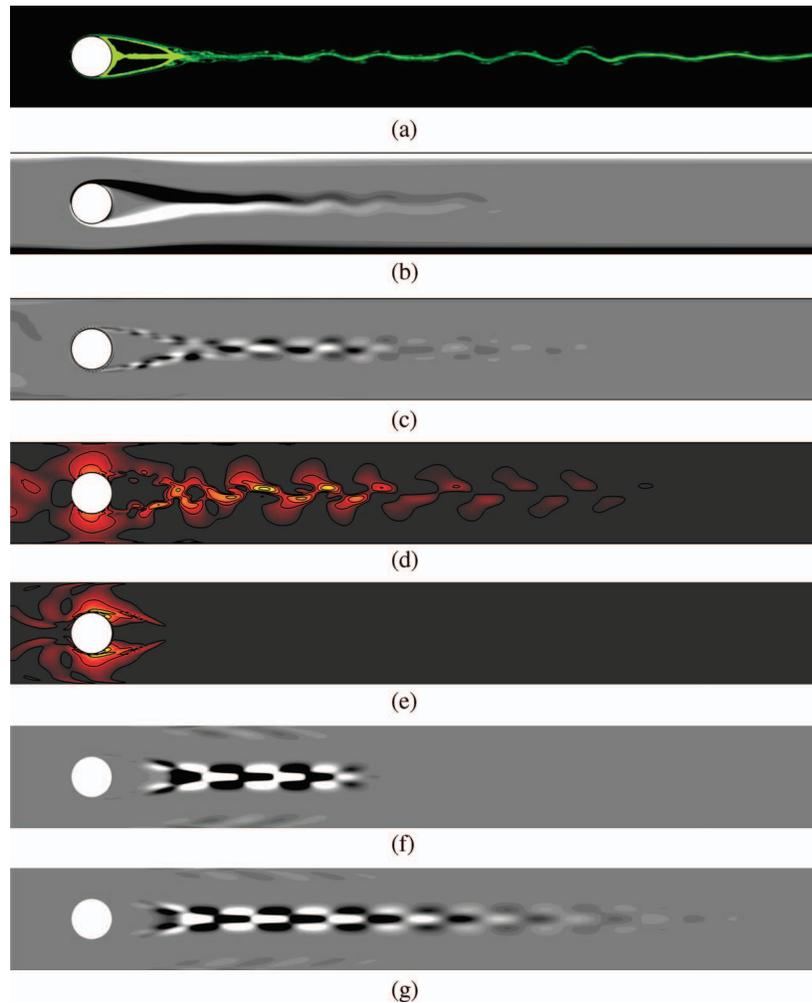
FIG. 17. (Color online) Plots visualizing a computation at $Re = 1160$, $Ha^\star = 200$, and $\beta = 0.4$ perturbed by a random disturbance at the inflow with an amplitude of up to $0.5U_0$. Frames show (a) simulated dye visualization of the disturbed flow; (b) the vorticity field of the disturbed flow; (c) the isolated disturbance vorticity as per Fig. 16; (d) the base-10 logarithm of the energy in the disturbance field shown in (c); (e) the base-10 logarithm of the energy of the optimal initial disturbance computed for evolution time τ_{max} for the unperturbed flow; (f) vorticity field of the linear optimal initial disturbance evolved to time $t = \tau_{max}$; and (g) vorticity in the leading global instability mode for the unperturbed flow obtained from a linear stability analysis. In each frame, arbitrary contour levels are plotted to elucidate the key features of the flow in each frame.

bubble a good agreement is observed across these three plots: alternating-sign vortex structures repeating at a consistent stream-wise wavelength are observed, which decay further downstream of the cylinder. The notable point of difference is that the white-noise disturbance field also features diverging zones of disturbance vorticity convecting from the flow separation points either side of the cylinder and into the wake. Whereas the optimal disturbance at τ_{max} and the global mode correspond to isolated disturbances in an otherwise unperturbed flow, the disturbance field is continuously fed by upstream disturbances. The visible disturbances in the separated shear layers appear as a result of this continuous injection of upstream disturbances, and reflect the amplifying nature of this region of the wake flow.

The energy field of the disturbance offers an added perspective on the perturbed flow, and is plotted in Fig. 17(d). Whereas the disturbance vorticity field compares favorably with that of the optimal growth mode evolved to time $t \approx \tau_{max}$, the energy fields are notably different. Firstly, the disturbance energy field exhibits a clear asymmetry about the centerline downstream of the cylinder. This asymmetry demonstrates that the disturbance has evolved to levels well beyond the

linear regime, and is consistent with the observed waviness in Figs. 17(a) and 17(b). Secondly, the disturbance energy field displays significant zones of energy either side of the cylinder, which is absent from the optimal disturbance energy plots in the vicinity of τ_{max} (see Fig. 12). This feature bears a close similarity to the energy field of the optimal initial condition, which is shown in Fig. 17(e). The interpretation to be drawn from this is that the weak inflow disturbances supply energy to the optimal transient modes in the flow, which in turn lead to amplification of the disturbances as they convect aft of the cylinder and into the wake. As the optimal mode has been shown to act as an amplifier for the global linear instability mode (as also seen in Ref. 35), these disturbances therefore manifest in a fashion consistent with the instability mode eventually leading to the von Kármán vortex street.

VI. CONCLUSIONS

An investigation has been carried out into the transient growth of optimal linear perturbations of a liquid metal magneto-hydrodynamic flow past a confined cylinder in a duct under a strong axial magnetic field in the subcritical regime prior the onset of oscillations. Under these conditions, the flow is quasi-two-dimensional and the modified Navier–Stokes equations are solved in a two-dimensional domain. The majority of the numerical simulations has been performed over the range of $50 \leq Re \lesssim 2100$, modified Hartmann numbers $50 \leq Ha^{\star} \lesssim 500$, and blockage ratios $0.1 \leq \beta \leq 0.4$.

For small blockage ratio, the recirculation bubble was found to be visible up to some critical $Ha^{\star}$. Beyond which it is suppressed due to the effect of the Lorentz forces, which produces a force in the direction opposite the flow resulting in the decrease of the wake length. The recirculation length, Reynolds number, Hartmann number, and blockage ratio were related as $L_R/d + 0.709 \propto Re^{0.844} Ha^{\star -0.711} \beta^{0.166}$.

For all blockage ratios, for a given Reynolds number, very significant transient energy growth was found in this regime, which suggests a potential for the design of actuation mechanisms to promote vortex shedding and thus enhance heat transfer in these ducts. The energy amplification of the disturbances was found to decrease significantly with increasing Hartmann number, and the growth peaks at shorter time intervals. This is due to the reduction of perturbation kinetic energy by Hartmann damping. The global maxima of energy was found to vary significantly with blockage ratio, being longer at higher β. The structure of the disturbance was found to be consistent across all the blockage ratios being tested.

The optimal disturbance was maximal in the region of the boundary layer separation around the cylinder in the near wake. The perturbation amplifies as it convects along the separating region being amplified to the peak growth state downstream of the recirculation bubble. The τ_{max} was found to increase significantly as recirculation length increases, which demonstrates the amplifying nature of the separated shear layers in the wake consistent with many other studies.

For all Re at high Hartmann number, it was found that increasing β leads to a significant increase of the energy amplification and to shift the global maxima towards smaller times.

The critical Reynolds number for positive energy growth of the optimal disturbance, Re_{c1}, was found to increase significantly with increasing blockage ratio and modified Hartmann number. The optimal disturbances at $Re \leq Re_{c1}$ monotonically decreased with τ, while for $Re \geq Re_{c1}$ the energy of an optimal disturbance increases rather than decreases from its initial value. For low Hartmann number, it was found that $\log G_{max}$ grows initially faster than linearly, approaching a linear variation with Reynolds number for Re significantly greater than Re_{c1}. This is true for all blockage ratios. On the other hand, for higher Hartmann number the growth becomes linear for Reynolds numbers not too far in excess of Re_{c1}.

Direct numerical simulations in which the inflow was perturbed by white noise demonstrated that the optimal transient growth properties of the flow could be activated by continuous upstream random perturbations, which resulted in a significant amplification of the disturbances as they passed around the cylinder. This was sufficient to destabilize the wake through the global instability responsible for producing the von Kármán wake, despite the simulation being run at conditions below the critical Reynolds number for vortex shedding.

[1] S. Münevver, "Magnetohydrodynamic flow in a rectangular duct," Int. J. Numer. Methods Fluids **7**, 697 (1987).

[2] I. R. Kirillov, C. B. Reed, L. Barleon, and K. Miyazaki, "Present understanding of MHD and heat transfer phenomena for liquid metal blankets," Fusion Eng. Des. **27**, 553 (1995).

[3] O. A. Lielausis, "Liquid-metal magnetohydrodynamics," At. Energy Rev. **13**, 527 (1975).

[4] L. G. Kit, S. V. Turuntaev, and A. B. Tsinober, "Investigation with a conduction anemometer of the effect of a magnetic field on disturbances in the wake of a cylinder," Magnetohydrodynamics **6**(3), 331 (1970).

[5] Yu. B. Kolesnikov and A. B. Tsinober, "Two-dimensional turbulent flow behind a circular cylinder," Magnetohydrodynamics **8**(3), 300 (1972).

[6] D. Papailio, "Turbulent magneto-fluid-mechanic vortex streets," Bull. Amer. Phys. Soc. **18**(11), 1484 (1973).

[7] M. Frank, L. Barleon, and U. Muller, "Visual analysis of two-dimensional magnetohydrodynamics," Phys. Fluids **13**, 2287 (2001).

[8] B. Muck, C. Gunther, U. Muller, and L. Buhler, "Three-dimensional MHD flows in rectangular ducts with internal obstacles," J. Fluid Mech. **418**, 265 (2000).

[9] V. Dousset and A. Pothérat, "Numerical simulations of a cylinder wake under a strong axial magnetic field," Phys. Fluids **20**, 017104 (2008).

[10] W. K. Hussam, M. C. Thompson, and G. J. Sheard, "Dynamics and heat transfer in a quasi-two-dimensional MHD flow past a circular cylinder in a duct at high Hartmann number," Int. J. Heat Mass Transfer **54**, 1091 (2011).

[11] L. Barleon, U. Burr, R. Stieglitz, and M. Frank, "Heat transfer of a MHD flow in a rectangular duct," in *Transfer Phenomena in Magnetohydrodynamic and Electroconducting Flows: Selected Papers of the PAMIR Conference held in Aussois, France, 22-26 September 1997*, Fluid Mechanics and its Applications Vol. 51, edited by A. Alemany, P. Marty, and J. P. Thibault (Kluwer, Aussois, France, 1997), pp. 305–309.

[12] J. A. Shercliff, "Some duct flow problems at high Hartmann number," Z. Angew. Math. Phys. **26**, 537 (1975).

[13] P. A. Davidson, "The role of angular momentum in the magnetic damping of turbulence," J. Fluid Mech. **336**, 123 (1997).

[14] A. Pothérat, J. Sommeria, and R. Moreau, "An effective two-dimensional model for MHD flows with transverse magnetic field," J. Fluid Mech. **424**, 75 (2000).

[15] J. Sommeria and R. Moreau, "Why, how, and when, MHD turbulence becomes two-dimensional," J. Fluid Mech. **118**, 507 (1982).

[16] T. Alboussiere, V. Uspenski, and R. Moreau, "Quasi-2D MHD turbulent shear layers," Exp. Therm. Fluid Sci. **20**, 19 (1999).

[17] O. V. Andreev and Y. Kolesnikov, "MHD instabilities at transverse flow around a circular cylinder in an axial magnetic field," in *Transfer Phenomena in Magnetohydrodynamic and Electroconducting Flows: Selected Papers of the PAMIR Conference held in Aussois, France, 22–26 September, 1997*, Fluid Mechanics and its Applications Vol. 51, edited by A. Alemany, P. Marty, and J. P. Thibault (Kluwer, Aussois, France), pp. 205–210.

[18] U. Burr, L. Barleon, U. Muller, and A. Tsinober, "Turbulent transport of momentum and heat in magnetohydrodynamic rectangular duct flow with strong sidewall jets," J. Fluid Mech. **406**, 247 (2000).

[19] R. Klein, A. Pothérat, and A. Alferenok, "Experiment on a confined electrically driven vortex pair," Phys. Rev. E **79**, 016304 (2009).

[20] L. Buhler, "Instabilities in quasi-two-dimensional magnetohydrodynamic flows," J. Fluid Mech. **326**, 125 (1996).

[21] Y. B. Kolesnikov and A. B. Tsinober, "Experimental investigation of two-dimensional turbulence behind a grid," Fluid Dyn. **9**, 621 (1974).

[22] J. Moreau and R. Sommeria, "Electrically driven vortices in a strong magnetic field," J. Fluid Mech. **189**, 553 (1988).

[23] P. J. Schmid and D. S. Henningson, *Stability and Transition in Shear Flows* (Springer, New York, 2001).

[24] S. C. Reddy, P. J. Schmid, J. S. Baggett, and D. S. Henningson, "On stability of streamwise streaks and transition thresholds in plane channel flows," J. Fluid Mech. **365**, 269 (1998).

[25] O. Y. Zikanov, "On the instability of pipe Poiseuille flow," Phys. Fluids **8**, 2923 (1996).

[26] D. Biau, H. Soueid, and A. Bottaro, "Transition to turbulence in duct flow," J. Fluid Mech. **596**, 133 (2008).

[27] H. M. Blackburn, D. Barkley, and S. J. Sherwin, "Convective instability and transient growth in flow over a backward-facing step," J. Fluid Mech. **603**, 271 (2008).

[28] H. M. Blackburn, S. J. Sherwin, and D. Barkley, "Convective instability and transient growth in steady and pulsatile stenotic flows," J. Fluid Mech. **607**, 267 (2008).

[29] C. D. Cantwell, D. Barkley, and H. M. Blackburn, "Transient growth analysis of flow through a sudden expansion in a circular pipe," Phys. Fluids **22**, 1 (2010).

[30] M. D. Griffith, M. C. Thompson, T. Leweke, and K. Hourigan, "Convective instability in steady stenotic flow: optimal transient growth and experimental observation," J. Fluid Mech. **655**, 504 (2010).

[31] J. M. Chomaz, "Global instabilities in spatially developing flows: Non-normality and nonlinearity," Annu. Rev. Fluid Mech. **37**, 357 (2005).

[32] F. Giannetti and P. Luchini, "Structural sensitivity of the first instability of the cylinder wake," J. Fluid Mech. **581**, 167 (2007).

[33] O. Marquet, D. Sipp, and L. Jacquin, "Sensitivity analysis and passive control of cylinder flow," J. Fluid Mech. **615**, 221 (2008).

[34] C. D. Cantwell and D. Barkley, "Computational study of subcritical response in flow past a circular cylinder," Phys. Rev. E **82**, 026315 (2010).

[35] N. Abdessemed, A. S. Sharma, S. J. Sherwin, and V. Theofilis, "Transient growth analysis of the flow past a circular cylinder," Phys. Fluids **21**, 044103 (2009).

[36] C. Marais, R. Godoy-Diana, D. Barkley, and J. Wesfreid, "Convective instability in inhomogeneous media impulse response in the subcritical cylinder wake," Phys. Fluids **23**, 014104 (2011).

[37] D. Gerard-Varet, "Amplification of small perturbations in a Hartmann layer," Phys. Fluids **14**, 1458 (2002).

[38] C. Airiau and M. Castets, "On the amplification of small disturbances in a channel flow with a normal magnetic field," Phys. Fluids **16**, 2991 (2004).

[39] D. S. Krasnov, E. Zienicke, O. Zikanov, T. Boeck, and A. Thess, "Numerical study of the instability of the Hartmann layer," J. Fluid Mech. **504**, 183 (2004).

[40] T. Boeck, D. Krasnov, M. Rossi, and O. Zikanov, "Transient growth in MHD duct flow," in *Advances in Turbulence XXII: Proceedings of the 12th EUROMECH European Turbulence Conference, September 7–10, 2009, Marburg, Germany*, Springer Proceedings Physics Vol. 132, edited by B. Eckhardt (Springer, Berlin, 2009), pp. 829–832.

[41] D. Krasnov, O. Zikanov, M. Rossi, and T. Boeck, "Optimal linear growth in magnetohydrodynamic duct flow," J. Fluid Mech. **653**, 273 (2010).

[42] D. Barkley, H. M. Blackburn, and S. J. Sherwin, "Direct optimal growth analysis for timesteppers," Int. J. Numer. Methods Fluids **57**, 1435 (2008).

[43] G. J. Sheard, M. J. Fitzgerald, and K. Ryan, "Cylinders with square cross-section: Wake instabilities with incidence angle variation," J. Fluid Mech. **630**, 43 (2009).

[44] H. M. Blackburn and G. J. Sheard, "On quasi-periodic and subharmonic Floquet wake instabilities," Phys. Fluids **22**, 031701 (2010).

[45] G. J. Sheard, T. Leweke, M. C. Thompson, and K. Hourigan, "Flow around an impulsively arrested circular cylinder," Phys. Fluids **19**, 083601 (2007).

[46] G. J. Sheard and M. P. King, "Horizontal convection: Effect of aspect ratio on Rayleigh-number scaling and stability," Appl. Math. Model. **35**, 1647 (2011).

[47] R. J. Moreau, *Magnetohydrodynamics* (Kluwer, Dordrecht, Boston, 1990).

[48] G. E. Karniadakis, M. Israeli, and S. A. Orszag, "High-order splitting methods for the incompressible Navier–Stokes equations," J. Comput. Phys. **97**, 414 (1991).

[49] G. J. Sheard, "Wake stability features behind a square cylinder: Focus on small incidence angles," J. Fluids Struct. **27**, 734 (2011).

[50] D. C. Hill, "A theoretical approach for analyzing the restabilization of wakes," in *30th AIAA Aerospace Science Meeting and Exhibit* (National Aeronautics and Space Administration, Ames Research Center/National Technical Information Service, Moffett Field, CA, USA/Reno, NV, USA, 1992), AIAA Paper No. 92-0067.

[51] N. Abdessemed, S. J. Sherwin, and V. Theofilis, "Linear instability analysis of low-pressure turbine flows," J. Fluid Mech. **628**, 57 (2009).

[52] G. J. Sheard, "Flow dynamics and wall shear-stress variation in a fusiform aneurysm," J. Eng. Math. **64**, 379 (2009).

[53] A. Neild, T. W. Ng, G. J. Sheard, M. Powers, and S. Oberti, "Swirl mixing at microfluidic junctions due to low frequency side channel fluidic perturbations," Sens. Actuators B **150**, 811 (2010).

[54] G. Coppola, S. J. Sherwin, and J. Peiró, "Nonlinear particle tracking for high-order elements," J. Comput. Phys. **172**, 356 (2001).